www.lajss.org
Latin American Journal of Solids and Structures 4 (2007) 121–147

Linear analysis of axis-symmetric plates and shells by the generalized Finite Element Method

Oscar Alfredo Garcia and Sergio Persival Baroncini Proença*

Structural Engineering Department, School of Engineering at São Carlos
University of São Paulo, SP – Brazil

Abstract

This paper is aimed at proving the ability of generalized finite element approximation spaces in dealing with axis-symmetric plate and shells problems. The GFEM is implemented using a degenerated shell element mesh [1] specialized for the axisymmetric case. The first order kinematic model of Reissner-Mindlin is adopted. Both h and hp-adaptivity are explored in the examples. The locking issue is analyzed through circular plate and revolution shell bending problems. The ability to approximate strong gradients in boundary layers is also shown by cylindrical revolution shell example. The enrichment over a cubic partition of unity is finally explored in order to reproduce smooth distributions of internal moments and shear forces.

Keywords: GFEM, axisymmetric shells, locking, boundary layer.

1 Introduction

The search for alternative approaches that provide a solution to problems of mechanics with reduced computational work has motivated an increasing interest for the so-called non-conventional numerical methods. In particular, much effort has been directed to the development of methods which ease the construction of more flexible approximation spaces involving a relatively small number of degrees of freedom and capable of addressing situations comprising highly localized gradients for unknown functions.

Spaces with the characteristics described above can be obtained by numerical techniques that dispend meshing ('meshless') such as: 'Multiquadric' ([7]); 'Reproducing Kernel Particle Method' (RKPM) [11]; 'Element Free Galerkin' (EFG) [3]; 'hp-Clouds' [5]; 'The Partition of Unity Finite Element Method' (PUFEM) [12], among others.

The Generalized Finite Element Method, GFEM, had its origin, simultaneously, from the hp-Clouds and the (PUFEM), by combining the ease of imposing essentials boundary conditions characteristic of FEM with the advantages offered by meshless methods. One such outstanding advantage is the possibility of defining the enrichment functions in the real domain of the problem

*Corresp. author email: persival@sc.usp.br Received 1 Dec 2006; In revised form 7 Mar 2007

thus avoiding the inconveniences caused by mesh distortion. The approach resulting from this combination can be defined as a generalization of the h, p and hp versions of conventional FEM.

The GFEM was first presented with this denomination and its mathematical formulation formally accessed in the work of (Duarte, Babuska and Oden, [4]). Despite its surprising performance in solving a wide range of problems of computational mechanics, the use of GFEM to the analysis of shell structures faces limitations. This is due mainly to limitations of its structure originating from the inexistence of an adequate systematic approach in the construction of approximation spaces when considering curved domains and a loss of competitiveness with respect to the p version of FEM for reasons that it demands high processing time.

On the other hand, the structural analysis of shell structures using the GFEM should maintain similarities to approaches employing methods without mesh. Because of this and also given the reduced number of research works on the application of GFEM to shell structures, a brief bibliographical revision covering shell analysis by meshless methods is here presented.

The first prominent contribution is given by (Krysl and Belytschko, [9]), in which thin shell structures are modeled using the moving least squares method (MLSM) to approximate the geometry and (EFG) to construct the approximation space. Another proposal is presented in the work of (Li et alli, [10]) which uses a meshless method (3D-RKPM) in modeling large deformations in thin shells. (Liew, Ng, Zhao and Reddy, [14]) and (Zhao, Ng and Liew, [17]) use a mixed method to process dynamic analyses of cylindrical shell. In their procedure, they combine a known solution in the direction tangent to the parallel and RKPM in the meridian direction.

The present work addresses the application of the GFEM in the analysis of plates and shells. The treatment presented is however, limited to the case of axis-symmetric configurations in structural geometry and loading. When focusing on low cost computational analysis, this modeling approach furnishes an easy means of evaluating the advantages offered by the GFEM. In this way, a versatile systematic is particularly adopted in constructing the enrichment of the approximation space in axis-symmetric curved domains. Essentially, the enrichment is carried out directly on the arch which defines the geometry of the solid represented in a parameterized domain.

In spite of the simplification derived from axis-symmetry, the approach tries to include shear deformation by using the first order Reissner-Mindlin kinematic model. The shell geometry is described by clouds defined from a mesh of axis-symmetric elements. These elements are derived from degenerated solid element concept proposed by Ahmad et al., [1]. The selected numerical examples underline the capacity of the GFEM both in overcoming the locking phenomena and in efficiently solving problems whose solutions present strongly localized gradients.

The content of the present text addresses the following topics: a brief description of the basic mathematical aspects of constructing approximation spaces on a parametric domain using the GFEM; the axis-symmetric solid element used to define clouds and the partition of unity; numerical examples and conclusions.

2 The aproximation space according to the GFEM

The generalized finite element method is based on methodologies in which the approximation space is constructed by enrichment of the partition of unity, that is, by its product with functions of a local approximation space.

The partition of unity is composed of functions φ_α defined on local supports or clouds ω_α, as illustrated in figure 1 for the one-dimensional case. On the other hand, functions within the local approximation space can be combinations of bases polynomials or space functions having characteristics of the solution itself when known.

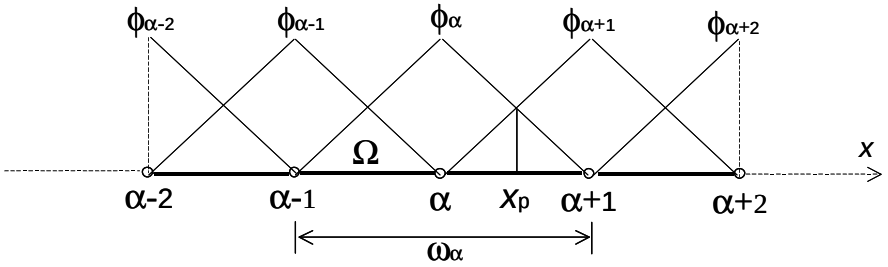

Figure 1: Partition of unity $\{\phi_\alpha(x)\}_{\alpha=1}^{N}$ on an open covering $\{\omega_\alpha\}_{\alpha=1}^{N}$.

Let, then $\{\omega_\alpha\}_{\alpha=1}^{N}$ be an open covering of the domain Ω, N being the number of clouds which comprises it and $\bar{\Omega} \subset \{\omega_\alpha\}_{\alpha=1}^{N}$ the closure of Ω. Still, let $\{\phi_\alpha\}_{\alpha=1}^{N}$ be a Lipschitz (Melenk and Babuska [12]) type partition of the unity subordinate to the covering (Figure 1). With the support defined in each sub-domain ω_α, the space Q_α assembles functions with good characteristics of local approximation and can be used to enrich the partition of unity. The set that assembles the local enriched approximations is then given by:

$$F_N^p = \{\{\phi_\alpha Q_\alpha\} : \ 1 \leq \alpha \leq \mathrm{N}\}; \tag{1}$$

The local spaces Q_α are in general constructed using base polynomials due mainly to their good efficiency in approximation and the ease of application to a wide variety of boundary value problems. To better characterize the use of polynomial bases in the local approximation space, hence to distinguish it from other possible polynomial bases, it become necessary to use the representation Q_α^p, where p denotes the maximum degree of the polynomial bases used in the approximation. Formally such a space can be indicated in the form:

$$Q_\alpha^p = \{L_{i\alpha}(\bar{x}) : \ 0 \leq i \leq p\}. \tag{2}$$

In (2), $L_{i\alpha}(.)$ is a set of polynomial bases which includes unity ($L_{o\alpha}(\bar{x}) = 1$) and $\bar{x}$ is a defined coordinate on the local support. More specifically, the abscissa $\bar{x}$ is referenced to the base node or local origin of the cloud ω_α, as indicated in Fig. 2. Such an abscissa can be obtained by a

simple coordinate translation process given by:

$$\bar{x} = x - x_\alpha \tag{3}$$

where x is the position of the point on the cloud ω_α and x_α the corresponding position of the base node, both measured in global coordinates.

The set F_N^p which assembles all enrichments linked to each cloud, on the other hand, becomes:

$$F_N^p = \{\{\phi_\alpha Q_\alpha^p\} : \ 1 \leq \alpha \leq \mathrm{N}\}, \tag{4}$$

Considering that the most simple partition of unity is composed of functions linear by parts, the dimension of the enriched local space generated by Q_α^p is given by $\dim(span\,\{Q_\alpha^p\}) = p+1$. Those spaces obtained in this way always contain complete polynomials, that is, they show the property: $P \subset F^p$, where P is the set of complete polynomials of degree $g \leq p+1$ (*Theorem 3.4*) (Duarte and Oden, [5]). The global approximation constructed using the partition of unity to paste together the local approximations inherits the properties of these approximations inside each cloud but with continuity given by the partition of unity (*Theorem 3.2*) (Melenk and Babuska, [12]).

The convergence of the numerical to the exact solution can be attained by refinement h, p and hp. Besides, whenever convenient, it is possible to explore the construction of optimum local spaces obtained by including special functions in Q_α.

On the other hand, it may be convenient to work with enrichment functions in $(\hat{\omega}_\alpha)$ clouds defined on normalized domains as:

$$\hat{\omega}_\alpha = \{\xi \in \mathrm{R} : |\xi|_{\mathrm{R}} \leq 1\}; \tag{5}$$

The domain $\hat{\omega}_\alpha$ is obtained by normalizing the abscissa $\bar{x}$ in relationship to a characteristic dimension, h_α as illustrated by Fig. 2. Such normalization is obtained formally from mapping $C_\alpha^{-1} : \bar{x} \to \xi$ such that:

$$\xi = \frac{\bar{x}}{h_\alpha}. \tag{6}$$

From where it is deduced that: $\bar{x} = h_\alpha \xi$.

In that way, the set of functions $L_{i\alpha}(\bar{x})$ and its gradient $\nabla_{\bar{x}} L_{i\alpha}(\bar{x})$ in the normalized domain are now defined by the expressions:

$$L_{i\alpha}(\bar{x}) = \hat{L}_i(\xi) \circ C_\alpha^{-1}(\bar{x}); \tag{7}$$

$$\nabla_{\bar{x}} L_{i\alpha}(\bar{x}) = \frac{1}{h_\alpha} \nabla_\xi \hat{L}_i(\xi). \tag{8}$$

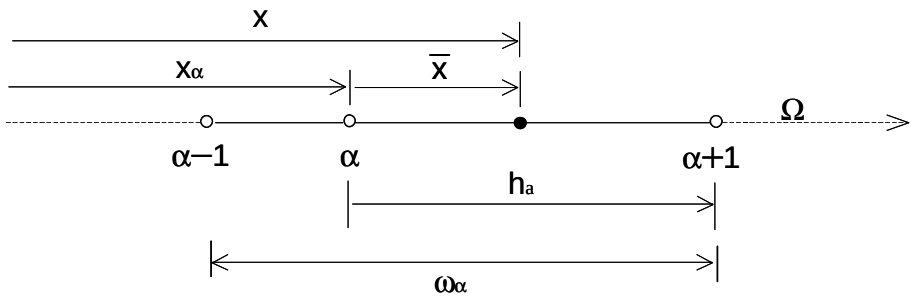

Figure 2: Local coordinate $\bar{x}$ from a x relative to a cloud α.

3 The local approximation space in the parameterized curved domain

The methodology adopted here permits the construction of approximations on curved physical domains described in an exact parametric manner when the equation of the curve is known or in an approximate form when the description is obtained by numerical techniques such as interpolation, minima least squares, etc.

Since the solids to be described are axis-symmetric, for convenience a system of cylindrical coordinates is adopted to represent a curve in the physical domain. Thus, the representation of the geometry will be made using curves contained in the (r-z) plane associated to the cylindrical coordinates system and positioned at an arbitrary angle θ relative to the axis X of the global reference in R^3, (as shown by Fig. 3).

What follow is a detail of the proposed methodology and a description of guidelines for the construction of enriched approximate functions. The basic idea of this procedure consists therefore, in constructing local approximations enriched directly on the parameterized physical domain. Concisely, a mapping composition that relates the natural domain (Ω_e) where the partition of unity is defined to a parameterized one-dimensional domain (Σ) and from this onto the physical domain of the problem is used.

The first mapping establishes then a relationship between points of a standard domain Ω_e (lineal, quadratic, cubic, etc.) on which natural coordinates are defined and points of a sub-domain in Σ (v.Fig. 3(b)). Formally we write:

$$\mathcal{C}_1(\eta) : \Omega_e \rightarrow x \in \{x \in \mathrm{R}/x_{i-1} \leq x \leq x_{i+1}\} \tag{9}$$

with $\Omega_e = \{\eta \in \mathrm{R}/-1 \leq \eta \leq 1\}$.

By definition, the function that accomplishes such a mapping constitutes, still, an isomorphism in $\Omega_e \rightarrow \{x \in \mathrm{R}/x_{i-1} \leq x \leq x_{i+1}\}$ since for each $\eta \in \Omega_e$there is only one $x \in \{x \in \mathrm{R}/x_{i-1} \leq x \leq x_{i+1}\}$. Besides, given $\eta_i \neq \eta_{i+1} \Rightarrow \mathcal{C}_1(\eta_i) \neq \mathcal{C}_1(\eta_{i+1})$. Later this property is also assumed to the second mapping, implying that the curves of the physical domain must be capable of being developed.

The mapping function $\mathcal{C}_1(\eta) : \Omega_e \rightarrow \{x \in \mathrm{R}/x_{i-1} \leq x_i \leq x_{i+1}\}$ can be composed of lagrangian polynomial functions defined in Ω_e. For the case of the mapping of quadratic functions for instance, a curve in Σ is constructed by interpolation of nodal values so that any position in that domain is determined by:

$$x = \sum_{i=1}^{3} N_i(\eta) x_i, \ i=1,...,3. \tag{10}$$

In (10), $N_i(\eta)$ are the classic quadratic functions of approximation associated to the natural domain:

$$\begin{aligned} N_1(\eta) &= -\frac{1}{2}\eta(1-\eta) \\ N_2(\eta) &= 1-\eta^2 \\ N_3(\eta) &= \frac{1}{2}\eta(1+\eta) \end{aligned} \tag{11}$$

Let $C(x) : \Sigma \rightarrow \mathrm{R}^3$, with $\Sigma = \{x \in \mathrm{R}/x_o \leq x \leq x_f\}$ then be a mapping that defines a curve in R^3 from a one-dimensional parametric domain which may be linear, quadratic, cubic, etc. Such a mapping therefore, relates each coordinate $x \in \Sigma$ to points on a plane curve whose cylindrical coordinates constitute components of the position vector $X(r,z,\theta) \in \mathrm{R}^3$, (v. Fig. 3b). It is admitted that the mapping is sufficiently regular in such a way that it generates a smooth curve.

For the specific case of a circumference arch, $x \in \Sigma = \left\{x \in \mathrm{R}/0 \leq x \leq \frac{\pi}{2}\right\}$ can be defined and $C(x)$ characterized parametrically by the following description of the vector components in cylindrical coordinates (for a fixed value of θ):

$$r(x) = R\cos(x); \tag{12}$$

$$z(x) = R\sin(x). \tag{13}$$

An interpretation of these relationships is shown in figure 3(a).

In particular certain points can be identified on the physical domain in correspondence to positions $x_i \in \Sigma$, such that:

$$r_i = R\cos(x_i) \tag{14}$$

$$z_i = R\sin(x_i) \tag{15}$$

More still, considering the case of the circumference arch as example and employing the mapping composition, the vector, $X(r,z,\theta) \in \mathrm{R}^3$ can be made to correspond directly to a certain position $\eta \in \Omega_e$ as shown below.

Initially, consider the vector $X(r,z,\theta)$ written as a linear combination of the unit vector $i_r(\theta)$ and k constituting the base of a cylindrical system (v.Fig. 3):

$$X(r,z,\theta) = r(x)\, i_r(\theta) + z(x)\, k; \tag{16}$$

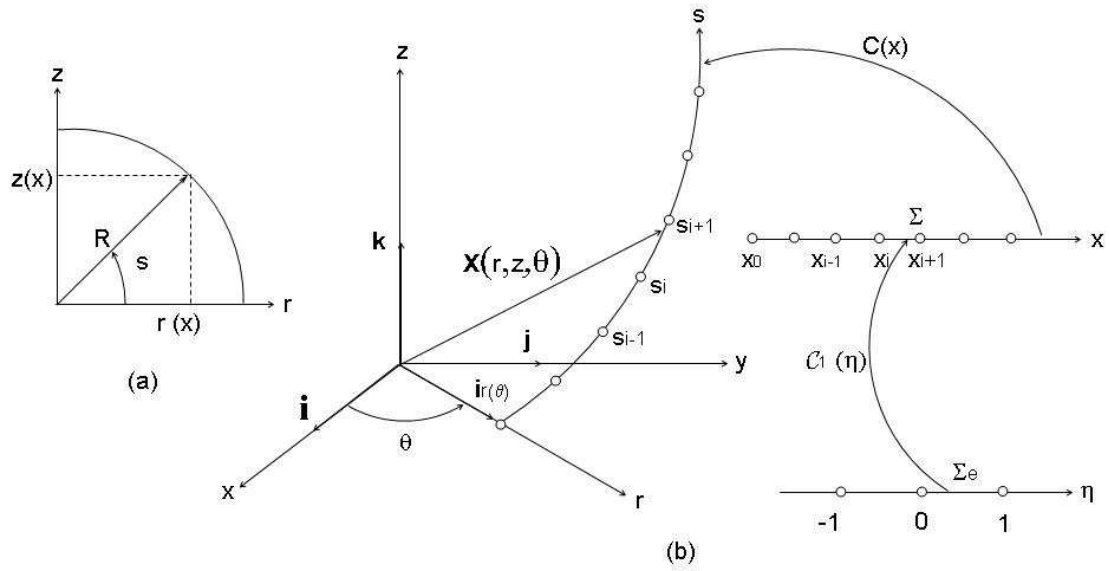

Figure 3: (a) Circumference curve in polar coordinates; (b) mapping of functions $C_1(\eta) : \Sigma_e \rightarrow x$ and $C(x) : \Sigma \rightarrow \mathsf{R}^3$.

The components $r\,(x)$ and $z\,(x)$ given in (12) and (13) can be expressed as a mapping function of the standard three-node domain Ω_e for instance. In that case, with the aid of the (10) we have:

$$r\,(x) = \sum_{i=1}^{3} N_i\,(\eta)\,r_i; \tag{17}$$

$$z\,(x) = \sum_{i=1}^{3} N_i\,(\eta)\,z_i; \tag{18}$$

In that way, (16) can be translated in terms of the functions $N_i\,(\eta)$ (for a fixed value of θ) as:

$$X\,(\eta,\theta) = \left[\sum_{i=1}^{3} N_i\,(\eta)\,r_i\right] i_r\,(\theta) + \left[\sum_{i=1}^{3} N_i\,(\eta)\,z_i\right] k \tag{19}$$

Once the geometry is defined, the enriched local approximation space can then be independently constructed on the one-dimensional parametric domain, Σ and later mapped onto the physical domain. This construction can be carried out over clouds defined by nodes occupying global positions x on the parametric domain Σ.

In order to take advantage of the benefits offered by non-dimensional coordinates a transformation of the parametric coordinates, x is initially carried out on each cloud. As presented in the previous section, such a transformation consists of translation relative to a local origin

defined in the base node of the cloud followed by normalization relative to the characteristic dimension, h_α as given by relationships (3) and (6).

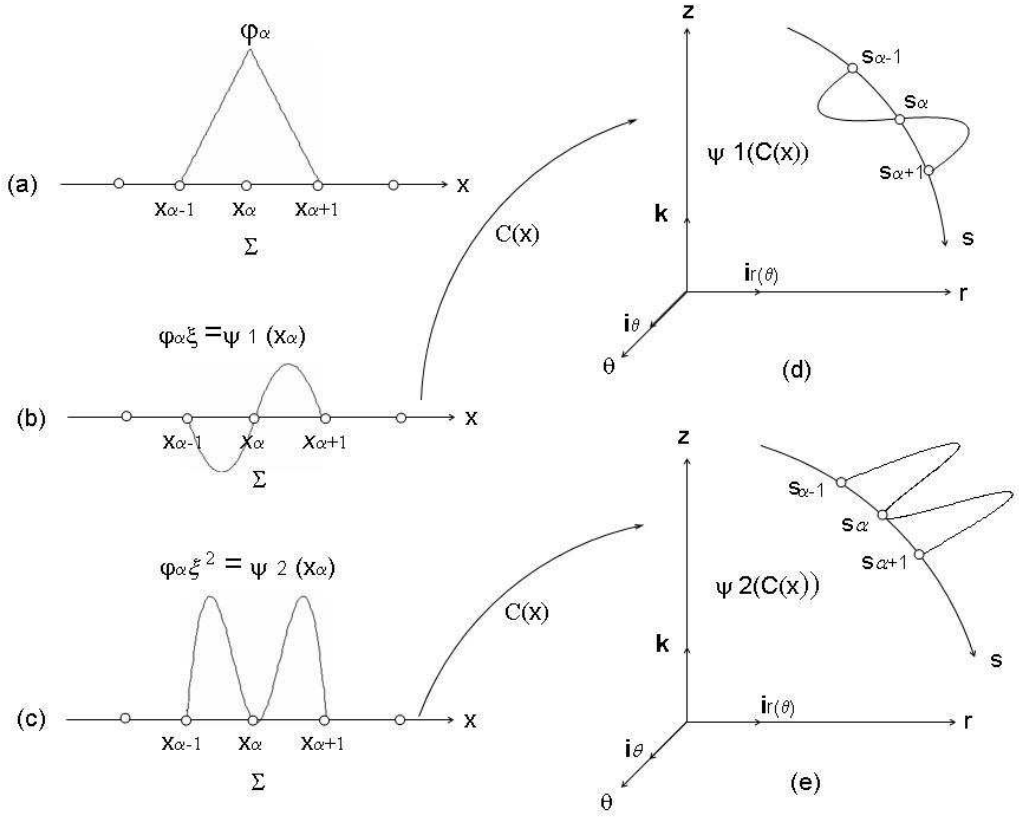

Figure 4: Approximation functions corresponding to cloud α.

In summary, the construction of the enriched local approximation space associated to the cloud α shown in Fig. 4 obeys the following sequence of operations:

a) The normalization of the $x \in \Sigma$ coordinate relative to the cloud local system characterized by: $x \in \{x \in \mathrm{R}/x_{\alpha-1} \leq x \leq x_{\alpha+1}\}$. The normalized coordinate ξ then results from:

$$\xi = \frac{x - x_\alpha}{h_\alpha}; \tag{20}$$

In expression (20), h_α is the larger of the distances obtained from $|x_{\alpha-1} - x_\alpha|$ and$|x_{\alpha+1} - x_\alpha|$.

b) The construction of the base for local enrichment and its derivative corresponding to the cloud α. For example:

$$\{L_2(\xi)\}_\alpha = \left\{1, \xi, \xi^2\right\}; \tag{21}$$

$$\left\{\frac{dL_2(\xi)}{d\xi}\right\}_\alpha = \{0, 1, 2\xi\}; \tag{22}$$

c) The construction of the local approximation space F_α^p enriched by product of partition of unity by the local space of enrichment, as indicated in the (4). Taking advantage of the example of the quadratic base, we obtain:

$$F_\alpha^2 = \{\psi_2(\eta)\}_\alpha = \left\{\phi_\alpha(\eta), \phi_\alpha(\eta)\,\xi, \phi_\alpha(\eta)\,\xi^2\right\}; \tag{23}$$

The partition of unity $\phi_\alpha(\eta)$ with continuity C^0 is formed by linear lagrangian functions (v.Fig. 4a) with the following definition:

$$\underset{-1\leq\eta\leq1}{\phi_\alpha(\eta)} = \begin{cases} N_1(\eta) = \frac{1}{2}(1+\eta)\ for\ x_{\alpha-1} \leq x \leq x_\alpha \\ N_2(\eta) = \frac{1}{2}(1-\eta)\ for\ x_\alpha \leq x \leq x_{\alpha+1} \end{cases} \tag{24}$$

Considering the correspondence between the x and η coordinates, a relationship similar to (10) is applied:

$$x = \begin{cases} N_1(\eta)x_{\alpha-1} + N_2(\eta)x_\alpha\ for\ x_{\alpha-1} \leq x \leq x_\alpha \\ N_1(\eta)x_\alpha + N_2(\eta)x_{\alpha+1}\ for\ x_\alpha \leq x \leq x_{\alpha+1} \end{cases} \tag{25}$$

The partition of unity and the set of functions defined in (23) for the example in question are represented in the parametric domain in Fig.4, (a), (b) and (c).

In some operations with the enriched functions, it may be necessary to multiply the gradient of the enrichment functions by that of the partition of unity. Since the partition is expressed in terms of natural coordinates, it is therefore more convenient to express the derivatives of the enrichment functions also in terms of the same coordinates. Hence:

$$\frac{d\hat{L}_i}{d\eta} = \frac{d\hat{L}_i}{d\xi}\frac{d\xi}{dx}\frac{dx}{d\eta}; \tag{26}$$

Since in (20) we conclude that $\frac{d\xi}{dx} = \frac{1}{h_\alpha}$, (26) may be redefined as:

$$\frac{d\hat{L}_i}{d\eta} = \frac{d\hat{L}_i}{d\xi}\frac{1}{h_\alpha}\frac{dx}{d\eta}; \tag{27}$$

Once the exact or approximate description of the curved physical domain is obtained, and hence, the mapping $C(x)$ is known, the above-described enrichment procedure, when extended to each cloud, permits the generation of the set of enriched approximations given in (4), but this time, on the domain in question. Figures 4 (d) and (e) show representations of the mapped enriched functions for a physical domain.

4 Axis-symmetric solid element

The approach presented in this section has the primary objective of developing sufficiently general tool to be applied to linear analysis of plates and shells showing axial symmetry in geometry and loading or prescribed deformation. Naturally, in order to apply GFEM, the

problem in question must be formulated in the weak form such that it satisfies equilibrium, compatibility and constitutive conditions of linear elasticity, all of which are specific for the axis-symmetric case (Timoshenko [16]). However, the variational formulation of boundary value problems is not the subject of the present work.

One characteristic of the GFEM is that a conventional finite element mesh can be employed in defining clouds that are linked to nodes. For the analysis of plates and shells developed in the present text, we will adopt clouds formed by degenerated solid-type elements proposed in (Ahmad et al., [1]), with its geometric description restricted to axis-symmetric problems according to Batoz and Dhat, [2]. Due to this restriction, on adopting a fixed value of $\theta = \bar{\theta}$, the element in the plane (r-Z) is fully described with the aid of the $i_r(\theta)$ and k unit vectors basis in the cylindrical coordinate system. In this plane, the projection (trace) of the mean surface is defined for a curved segment on which three element nodes are located (see Fig. 5). The position vector given by (16) turns out to correspond to points of that segment and with each node specifically.

In order to study the mapping from the master element, a local base with vectors $[v_{2k} : v_{3k} : i_\theta]$ is defined on node k (see Fig. 5).

Considering that the thickness of the solid, plate or shell is variable within the limits of the element, a certain variation of thickness can be represented by interpolating discrete values associated to each node. Based on this, a vector V_{3k} is defined for each node k whose absolute value corresponds to the local value of the thickness, t_k. With the aid of the illustration in Fig. 5, the following relationships are therefore valid:

$$V_{3k} = X_k^s - X_k^i \tag{28}$$

$$v_{3k} = \frac{V_{3k}}{|V_{3k}|} \tag{29}$$

with $|V_{3k}| = t_k$, $X_k^i\left(\bar{\theta}\right) = r_k^i i_r\left(\bar{\theta}\right) + z_k^i k$ and $X_k^s\left(\bar{\theta}\right) = r_k^s i_r\left(\bar{\theta}\right) + z_k^s k$.

The unit vector is obtained v_{2k} from the vector product of v_{3k} and i_θ (this being 'a priori' perpendicular to the (r-z) plane).

Once the local base is defined, it hence proceeds (according to Fig. 6) that a point, $\hat{X}$ in the direction v_{3k} with ordinate ζ in the element natural domain is obtained by linear interpolation of points X_k^s and X_k^i:

$$\hat{X}_k\left(\zeta, \bar{\theta}\right) = X_k^s N_s\left(\zeta\right) + X_k^i N_i\left(\zeta\right) \tag{30}$$

where,

$$\begin{aligned} N_s\left(\zeta\right) &= \frac{1}{2}\left(1 - \zeta\right) \\ N_i\left(\zeta\right) &= \frac{1}{2}\left(1 + \zeta\right) \end{aligned} \tag{31}$$

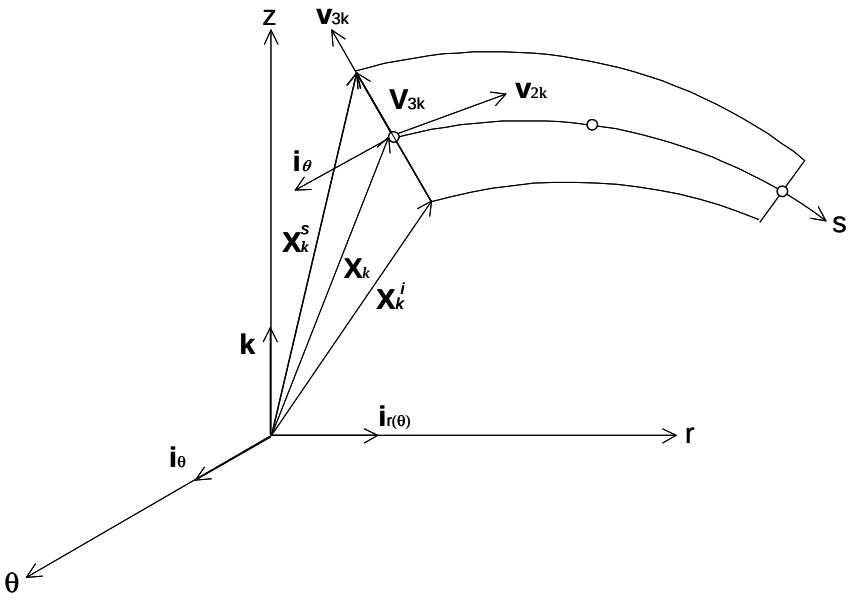

Figure 5: Geometry of the axis-symmetric solid element.

are linear functions of lagrangian interpolation. Considering the aforestated relationships, (30) can be expressed in still another form as:

$$\hat{X}_k\left(\zeta,\bar{\theta}\right) = X_k\left(\bar{\theta}\right) + v_{3k}\left(\bar{\theta}\right)\frac{t_k}{2}\zeta \tag{32}$$

with $X_k\left(\zeta,\bar{\theta}\right) = \frac{X_k^s\left(\bar{\theta}\right)+X_k^i\left(\bar{\theta}\right)}{2}$.

Finally, a generic point, $X\left(\eta,\zeta,\bar{\theta}\right)$, inside the element (see Fig. 6) is obtained by a second interpolation, but now, of values of $\hat{X}_k\left(\zeta,\bar{\theta}\right)$ determined for each node by applying (32). In this manner we have:

$$X\left(\eta,\zeta,\bar{\theta}\right) = \sum_{k=1}^{3} N_k\left(\eta\right)\hat{X}_k\left(\zeta,\bar{\theta}\right) \tag{33}$$

In expression (33), $N_k\left(\eta\right)$ are quadratic functions of lagrangian interpolation associated to each one of the three nodes.

Hence, the mapping of a point in the natural domain, Ω_e, onto its position vector in the (r-z) plane of the domain of the solid according to Fig. 6 is described by the expression:

$$\begin{aligned} X\left(\eta,\zeta,\bar{\theta}\right) = &\left[\sum_{i=1}^{3} N_i\left(\eta\right) r_i + \sum_{i=1}^{3} N_i\left(\eta\right)\frac{t_i}{2}\zeta v_{3i}^r\right] i_r\left(\bar{\theta}\right) \\ &+ \left[\sum_{i=1}^{3} N_i\left(\eta\right) z_i + \sum_{i=1}^{3} N_i\left(\eta\right)\frac{t_i}{2}\zeta v_{3i}^z\right] k. \end{aligned} \tag{34}$$

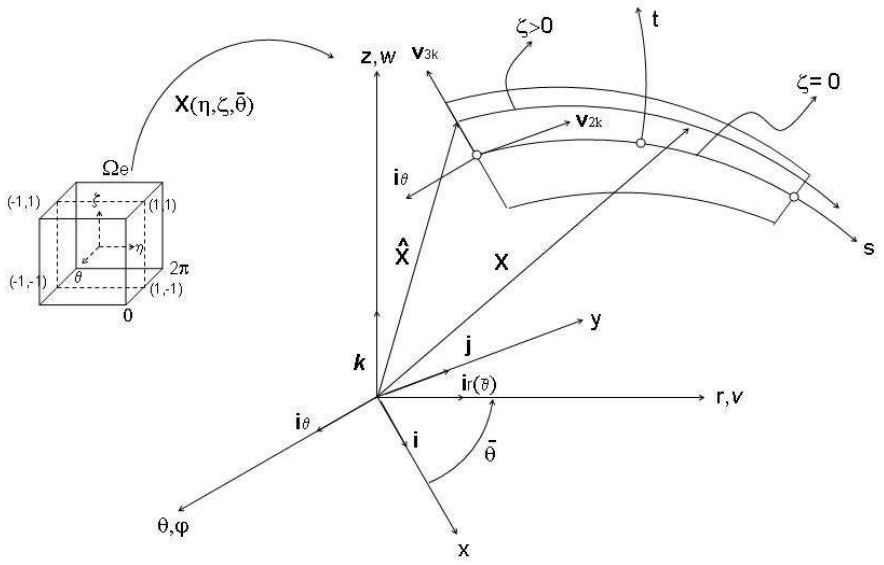

Figure 6: Mapping of the natural domain onto an axis-symmetric solid element.

It is easy to note that the relationship (19) can be thought of as a particularization of relationship (34) for a certain value of θ and natural coordinate $\zeta = 0$.

Another characteristic of GFEM is that the approximation spaces of the geometry and displacement fields are independent. In particular, in the present work, enrichments of the displacement fields are accomplished on axis-symmetric solid elements clouds whose base nodes are disposed on reference mid surface.

The kinematic model adopted to describe the deformation of the solid is the first order kinematic model of Reissner-Mindlin. This implies that the normal to the mid-surface is always straight during the deformation process and that the model takes into account a portion of the rotation corresponding to shear strain. A particularization of this kinematic model for the axis-symmetric solid element requires that three parameters or degrees of freedom be defined for each node k: displacement in the radial direction r; displacement, w_{ok} in the global direction z; and the rotation, φ_k about $i_{\bar{\theta}}$.

On the other hand, the definition of the displacement vector of a generic point is based on a similar procedure to that used in describing the geometry, that is: the interpolation of nodal displacements.

Firstly, the displacement vector of a point along the thickness on node k is determined by linear interpolation of discreet values on the extremities of the thickness. Such a vector, written in the (r-z) plane as a linear combination of the unit base vector of the cylindrical coordinates

system results in:

$$\hat{u}_k\left(\zeta,\bar{\theta}\right)=\left(v_{ok}+\frac{t_k}{2}\zeta\varphi_k v_{2k}^r\right)i_r\left(\bar{\theta}\right)+\left(w_k+\frac{t_k}{2}\zeta\varphi_k v_{2k}^z\right)k \tag{35}$$

It is worth noting that the coefficients of the linear combination result from the coherence with the kinematic model, v_{2k}^r and v_{2k}^z being the components of the unit vector v_{2k} according to the base $(i_r(\theta)-k)$. The displacement of a point in the element is then obtained by interpolation of $\hat{u}_k\left(\zeta,\theta\right)$ obtained from (35) for each node of the element:

$$u\left(\eta,\zeta,\bar{\theta}\right)=\sum_{k=1}^{3}N_k\left(\eta\right)\hat{u}_k\left(\zeta,\bar{\theta}\right) \tag{36}$$

Finally, once the enriched local approximation space is represented in a similar manner to that described by (7), and still, considering contributions of all clouds which contain the given point instead of considering the element, the displacement vector is expressed by the relationship:

$$\begin{aligned}u=u_h\left(\eta,\zeta,\bar{\theta}\right)=&\left[\sum_{j=1}^{n}\left(\sum_{k=1}^{m}\psi_k^j\left(\eta\right)v_{ok}^j+\sum_{k=1}^{s}\psi_k^j\left(\eta\right)\frac{t_j}{2}\zeta\varphi_k^j v_{2j}^r\right)\right]i_r\left(\bar{\theta}\right)\\&+\left[\sum_{j=1}^{n}\left(\sum_{k=1}^{m}\psi_k^j\left(\eta\right)w_{ok}^j+\sum_{k=1}^{s}\psi_k^j\left(\eta\right)\frac{t_j}{2}\zeta\varphi_k^j v_{2j}^z\right)\right]k\end{aligned} \tag{37}$$

In Eq. (37), n and m are respectively the number of active nodes (base nodes of clouds that contain the given point) and the number of approximation functions used in enriching each active node. The terms, v_{ok}^j, w_{ok}^j and φ_k^j now become nodal parameters introduced by the enrichment with a given function k associated to a cloud j. The enriched nodal functions, $\psi_k^j\left(\eta\right)$ are obtained as exemplified by Eq. (23).

5 Examples of numeric application

The cases of axis-symmetric plates and shells considered here are aimed at illustrating the performance of approximation spaces constructed following the GFEM. Particularly, it is sought to explore advantages such as combining the *p* and *hp* strategies in order to overcome the problem of numeric locking and to adequately represent highly localized gradients of the solution including the so-called limit layer problems. The examples analyzed here constitute critical cases among the ' benchmarks' proposed in specific literatures.

For a geometric representation of the solids analyzed, use will be made of either quadratic elements (Q3) or circular arch elements (C3). In the first case, the mean surface is approximate for quadratic lagrangian functions using the mapping given by (10) and (11), while in the second case, the mean surface is exactly described.

5.1 The phenomenon of numeric locking

Approximation spaces usually employed in the Reissner-Mindlin first order kinematic model are unable to reproduce the nullity of the shear and of membrane strains when a decrease in thickness is imposed. Under these conditions, there is a resultant increase in bending (flexural) stiffness of the structure whose solution converges to more conservative values, characterizing the so-called numeric locking.

In general, it can be affirmed that the locking can get revealed whenever there is deterioration of the approximation space, be it due to a limitation in the degree of approximation, be it due to used of distorted meshes. It therefore proceeds that due to its characteristic p enrichment, the GFEM can make the approximation sufficiently flexible thus constituting a valuable tool for overcoming problems of numeric locking.

In the present work, locking is addressed through examples of circular plates fixed at its boundary and subjected to a uniformly distributed load, and a long cylindrical shell under punction by a traverse load applied in the radial direction. The examples always admit a homogeneous and isotropic material.

Locking is verified for different thicknesses by observing fields of maximum displacements normalized relative to analytic solutions (Timoshenko et al., [16]). When employing the GFEM, the enriched approximation space is constructed by a homogeneous p refinement (at all nodes) for the two analyzed examples.

Circular fixed plate

The example presented consists of a circular plate fixed along its boundary and subjected to self weight evenly distributed on its entire superior surface. By exploring axis-symmetry, emphasis will be given to the analysis of the radius AO (Figs. 7(a) and (b)) discretized using six elements Q3 shown in figure 7(c). The load q varies in intensity according to the thickness t such that the same transverse displacement w is obtained for all relationships $2R/t$. The geometric and mechanical properties of the plate are: radius $R = 800mm$; variable thickness t; modulus of elasticity $E = 2.1 \times 10^5 MPa$; Poisson coefficient $\nu = 0.3$.

The effects of locking are evaluated by comparing the numeric results obtained for the maximum traverse displacement, w, normalized with relationship to the analytic solution of thin plate (wa) for different relationships between the radius and semi-thickness ($2R/t$) (Timoshenko et al., [16]). Such results are due to the adoption of homogeneous p refinement to construct enriched approximation spaces thus generating polynomials orders of $p = 2$, $p = 3$ and $p = 4$. As it can be perceived, the same problem discretized in the R^2 space will usually presents locking (Garcia [9]).

The results shown in figure 8 indicate that locking occurs only for $p = 2$ and even so, only for certain relationships ($2R/t$). On enriching the approximation, this locking problem seems to be fully overcome.

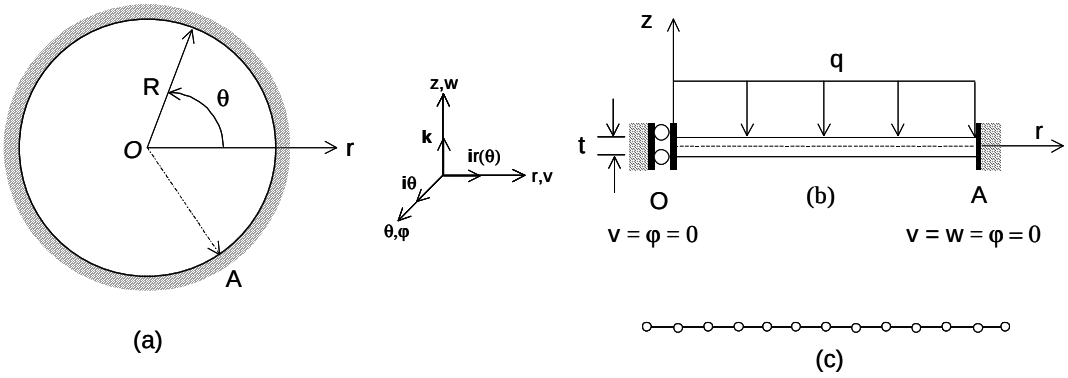

Figure 7: a) Fixed circular plate; b) Boundary conditions considering symmetry; c) Discretization of the radius OA using 6 $Q3$ elements.

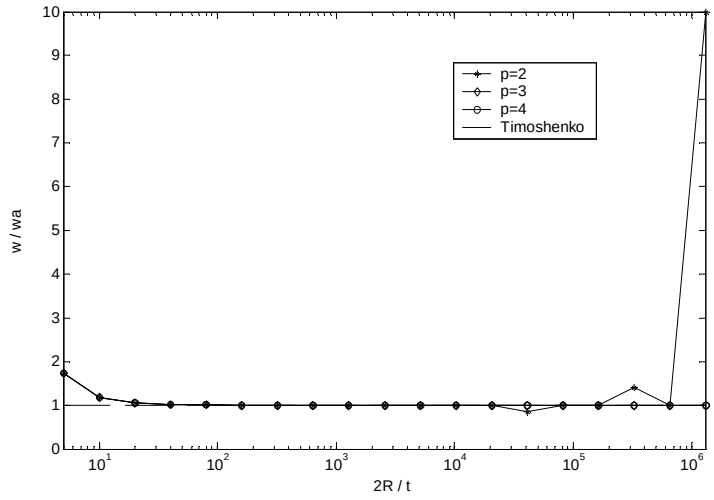

Figure 8: Values of transversal displacement w/wa normalized relative to $2R/t$.

Cylindrical tube under punction

A long cylindrical tube supported at its ends by diaphragms which do note restrict longitudinal displacement (see Fig. 9(a)) is subjected to a punction force (P) distributed along the line representing the mean height. The following geometric and mechanical properties are adopted: radius of cylinder, $R = 300mm$; variable thickness t; height, $H = 2400mm$; Young's modulus of elasticity, $E = 2.1 \times 10^5 MPa$; Poisson coefficient, $\nu = 0.3$.

Again, due to axis-symmetric properties, only the meridian segment OA is analyzed for the symmetric boundary conditions indicated in Fig. 9(b).

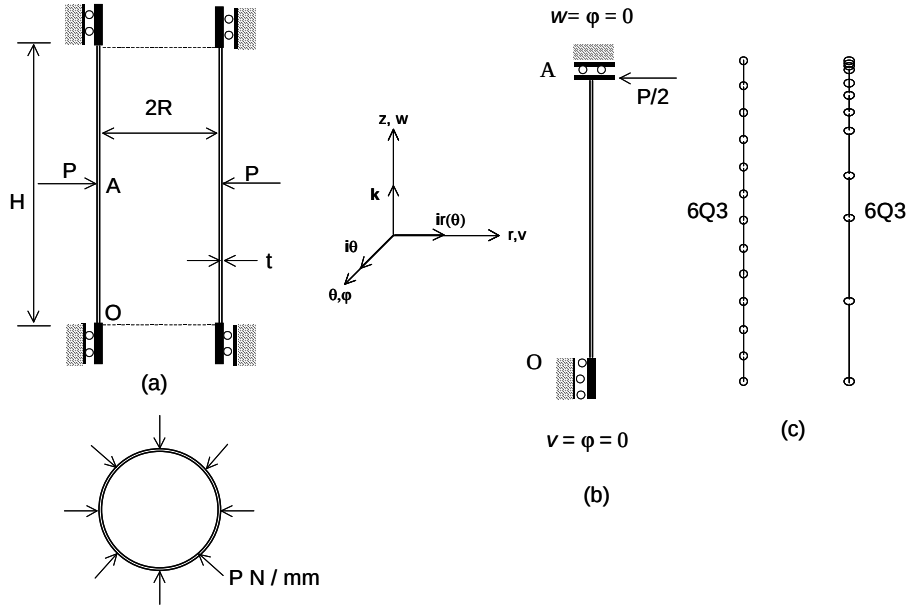

Figure 9: a) Fixed cylindrical tube under punction at $H/2$; b) Boundary conditions with symmetry respected; c) Discretization with regular and irregular mesh.

The deformation of the tube is dominated by bending mechanisms thus potentiating the effects of locking. Similarly to the previous case, locking is evaluated by comparing numeric results obtained for maximum radial displacement normalized with the analytic solution of a thin shell considering different radius-thickness, (R/t) relationships, (Timoshenko et al., [16]). Two solution strategies are adopted to overcome boundary locking:

1. Uniform mesh as shown in figure 9(c) and a homogeneous enrichment which generates polynomial degrees of $p = 2, ..., 4$.

2. A mesh whose geometric refinement progresses at a ratio of 2.5 in the direction of the applied force and homogeneously enriched, thus generating polynomial degrees $p = 2, ..., 4$ (see Figure 9(c)).

The results of the first strategy are shown in the figure 10(a) and indicate a fort locking slightly relieved by the enrichment of the approximation. Such results are expected since, according to Szabó and Babuska, [15], homogeneous p strategies associated to a crude mesh are not appropriate in solving problems whose solutions show strongly localized gradients. The second strategy, the hp combination, presents a more efficient result as figure 10(b) indicates. Notice that up to $R/t = 10^5$, locking is totally solved when $p = 4$.

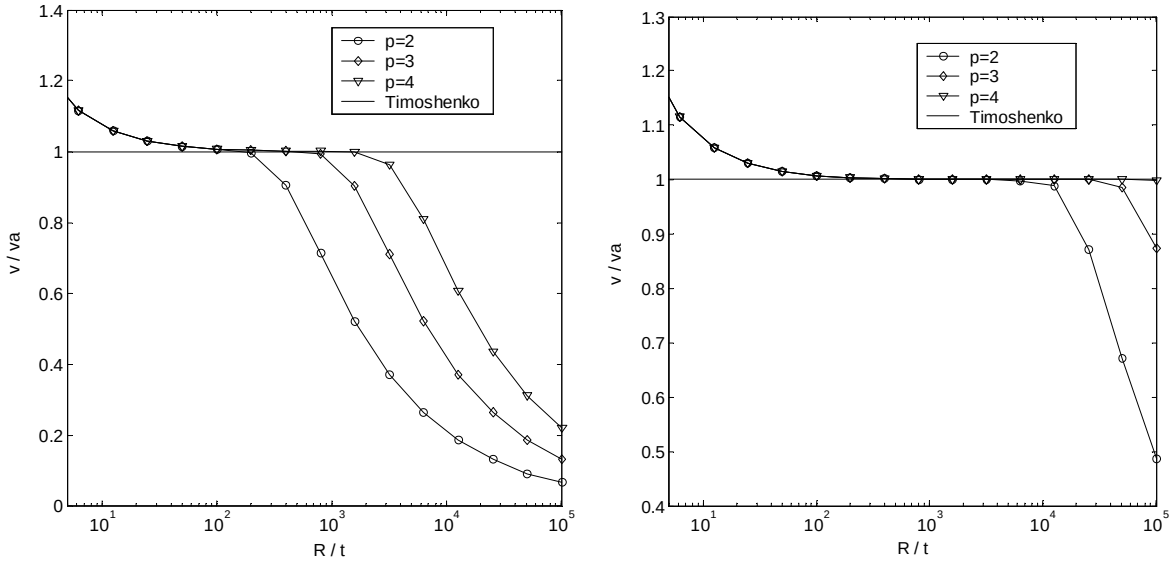

Figure 10: Radial normalized displacement v/va.

5.2 Other localized gradients and limit layer problems

The present section brings together problems involving localized gradients of solutions obtained for concentrated forces and problems directly related to the phenomena of limit layer.

Concerning the first type of problems, we show that the adaptive h strategies are really necessary. The combination of the h and p strategies provided by the GFEM can make the approach most efficient. Convergence aspects are analyzed by controlling the energy norm of the relative error in displacements.

On the other hand, with the recent use of non-conventional approximation methods, a notable improvement in approaching the limit layer type of problems has been seen. For instance, Garcia, [6], Da Nóbrega and Proença, [13] show that the employment of special functions which include solution modes may sometimes spare the need of adaptive h refinements in representing highly localized gradients of the solution. However, in the related examples here adjoined the alternative to be explored consists on enrichment of partitions of unity presenting continuity of

higher order. The advantage is to extend the continuity to the approximation of the internal efforts.

Circular plate with central hole

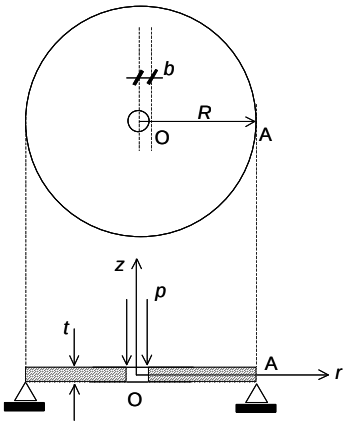

Figure 11: Circular plate with a central hole

This example consists of a simply supported circular plate with a central circular hole. A distributed load of $-1.0N/mm$ is applied perpendicularly to the plane of the plate along the internal circumference of the plate (see Fig. 11). The geometric and mechanics properties for this example are: radius of plate, $R = 800mm$; radius of the hole, $b = 0.8mm$; plate thickness, $t = 8.0mm$; modulus of elasticity, $E = 2.1 \times 10^5 MPa$; Poisson coefficient, $\nu = 0.3$.

This problem is one with peculiar regular characteristics. The solution presents a good regularity in most of the plate, but however, with a highly localized gradient although without singularity in the proximity of the hole. In this class of problems, the efficiency of polynomial approximations is quite limited if not complemented with the adaptive h and hp strategies (Szabo and Babuska, [15]). The main objective of the example is therefore to carry out convergence analyses with the degree of global approximation being varied both by mesh refinement and by the enrichment of the partition of unity. In this way, the relative errors in displacements estimated by the energy norm and expressed below are controlled. Therefore we have:

$$\|E_r\|_e = \frac{\|w_r - w\|_{E(\Omega)}}{\|w_r\|_{E(\Omega)}}; \tag{38}$$

In (38), w_r is a reference solution for traverse displacements and w the approximate solution corresponding to a specific strategy.

The reference solution w_r is obtained from the adaptive hp strategy made up of a mesh of 24 elements along the radius OA and whose length follows a geometric progression with factor $r = 0.5$ and decreasing in the direction of the hole. Since it is the intention that this solution

be better than the solutions obtained from subsequent strategies, polynomial enrichment on a partition of cubic unity is also carried out. In this manner, obtaining a smooth strain field is guaranteed. The p refinement for this case consists of the enrichment of the first twelve clouds that are adjacent to the hole using the following sequence of polynomial orders $p = \{2, 3, 4, 5, 6, 7, 8, 9, 10, 11, 12, 13\}$. The remaining clouds are enriched using $p = 13$ attaining a total of 810 degrees of freedom for the problem.

The analyses accomplished are for four discretization strategies:

1. The first, "Case A", constitutes nine meshes obtained from a uniform h refinement. Homogeneous polynomial enrichment with $p = 5$ is the applied on all the series of meshes used. The characteristics in terms of the number of elements used in each case and of the number of degrees of freedom are shown in Table 1. The efficiency of this strategy is evaluated by the behavior of the relative error $\|E_r\|_e$ estimated by Eq.(38), also shown in Table 1 and illustrated in Fig. 12a.

2. The second strategy, "Case B", is also made of an adaptive h refinement for each mesh using the same number of elements in the previous strategy, but however, distributed following a geometric progression with a fixed factor of $r = 0.55$ decreasing in the direction of the hole. The characteristics of this refinement are shown in Table 2. This table shows, in particular, the ratio of largest to the smallest element generated for each mesh, D/d. The results are presented in Table 2 in terms of the relative error and illustrated in Fig. 12a.

3. The third strategy, "Case C", is *hp*-adaptive obtained by a sequence of nine meshes of twelve elements Q3 disposed following a geometric progression which decreases in the direction of the hole and having progressive factors shown in the third column of Table 3. Associated to the adaptive h refine, a homogeneous p enrichment of increasing order as shown in Table 3 is successively applied.

4. The last strategy, "Case D", is also *hp*-adaptive, composed of a sequence meshes that is identical to that used in strategy "C". In this case, the advantage of selective adaptive p-refinement indicated in Table 4 is explored. The polynomial refinement is such that a quadratic enrichment is always applied to the first cloud adjacent to the hole (cloud number 12). For the next clouds whose numbering sequence is given in column three of Table 4, enrichments with linearly increasing orders of polynomial as indicated in column four of Table 4 are carried out. Finally, for the remaining clouds, polynomial orders indicated in column five of the same table are homogeneously applied.

The results obtained for the strategies: "Case C" and "Case D", are shown in Fig 12b.

The uniform $h-$refinement used in the case "A" (see Fig. 12a) presents a very low and linear rate of convergence since this strategy is not adequate to solve problems with highly localized gradients (Szabó and Babuska, [15]).

Table 1

N^o	Elem.Number	NDOF	$\|E_r\|_e$
1	6	126	7096.6099
2	8	162	4023.0563
3	10	198	2594.7340
4	12	234	1815.7733
5	14	270	1344.2314
6	16	306	1036.9820
7	18	342	825.5106
8	20	378	673.6587
9	22	414	560.8709

Table 2

N^o	Num.Elements	D / d	NDOF	$\|E_r\|_e$
1	6	19.8694	126	158.63173389
2	8	65.6842	162	18.808441617
3	10	217.1379	198	3.1523393763
4	12	717.8115	234	0.7248441339
5	14	2372.9305	270	0.1983855574
6	16	7844.3986	306	0.0580589824
7	18	25931.8964	342	0.0173400012
8	20	85725.2774	378	0.0051817160
9	22	283389.3471	414	0.0015219565

Table 3

N^o	Pol.Order	Geom. factor	NDOF	$\|E_r\|_e$
1	2	1.0	117	1815.34065
2	3	0.9	156	520.87000
3	4	0.8	195	103.32200
4	5	0.7	234	15.03468
5	6	0.6	273	1.980220
6	7	0.5	312	0.25866
7	8	0.4	351	0.02581
8	9	0.3	390	0.00154
9	10	0.17	429	0.00038805

Table 4

N^o	NDOF	$[C_i.,,,.C_j]$	$[P_i,..,P_j]$	Reman.Clouds Pol.Order	Geom. factor	$\|E_r\|_e$
1	180	12.,,,.10	2,...,4	4	1.0	1815.8167486
2	207	12.,,,.9	2,...,5	5	0.9	520.83196190
3	231	12.,,,.8	2,...,6	6	0.8	103.33057999
4	252	12.,,,.7	2,...,7	7	0.7	15.036046657
5	270	12.,,,.6	2,....,8	8	0.6	1.9804705673
6	285	12.,,,.5	2,...,9	9	0.5	0.2587675843
7	297	12.,,,.4	2,...,10	10	0.4	0.0252579350
8	306	12.,,,3	2,...,11	11	0.3	0.0011901489
9	312	12,...,2	2,...,12	12	0.17	0.0004273960

The h-adaptive strategy, where $D/d \to \infty$ when $d \to 0$, employed in case "B" is shown to be more robust than the previous case (see Fig. 12b). In fact, as the number of elements increases, the rate of convergence turns out to be independent of the smoothness of the problem (Szabó and Babuska, [15]), presenting values higher than those observed in the previous strategy.

Strategies "C" and "D" being hp-adaptive, combine positive characteristics of the h and p strategies thus reducing the errors in regions where the solution shows a low or a high regularity and provide higher rates of convergence. As a result of this combination, in both cases, the rates obtained were found to be exponential as it can be verified in Fig. 12b.

The strategy "C" shows a good performance, however, it can be noted that there is no ulterior improvement in the convergence rate for geometric factor from $D/d > 10^5$ (point 8). This is due to characteristics of the problem solution: essentially geometric meshes are well behaved in regions of localized gradients while an increase of the degree of the polynomial solution is more efficient in areas of smooth solution. From a certain level of geometric refinement, the h-adaptiveness attains its maximum efficiency, that is, the resulting rates of convergence turn out to be independent of the smoothness of the solution (Szabó and Babuska, [15]). However, since the degree of the polynomial adopted such that homogeneous enrichment could be maintained during all sequences, as soon as the ratio of the largest to smallest element became very high (elements of the region of the smooth solution were shown to be very high), the fixed order of the polynomial adopted was observed to be no longer efficient in this area, resulting in the stabilization or even an increase in the error.

Comparing the response obtained when employing strategy "C" to case "D", it can be concluded that the selective polynomial enrichment procedure, made possible by the GFEM, when applied to meshes refined following a geometric progression and from a certain degree of refinement, can sensibly reduce the error with a lower number of degrees of freedom (this

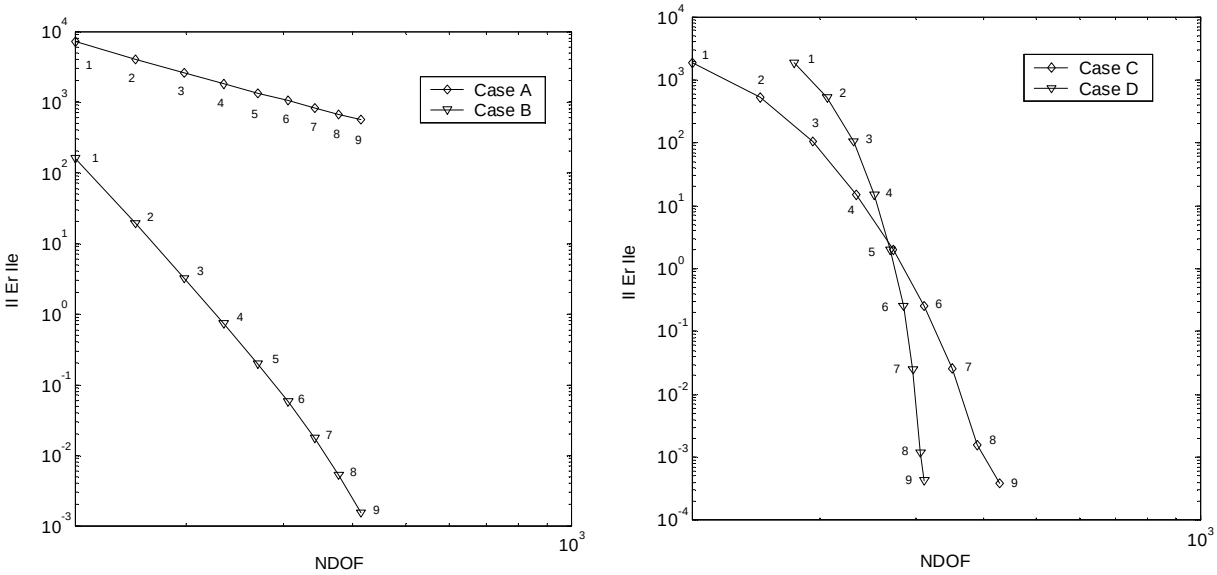

Figure 12: a) Case A, homogeneous h-refinement, Case B, adaptive h-refinement, b) Case C and Case D adaptive hp-refinement.

comparison can also be made by analysis of the tables 3 and 4).

The thin walled cylindrical tube under uniform internal pressure

In this case, we search to evidence the good capacity of representing boundary layer phenomena by approximation spaces constructed following the p-adaptive GFEM procedure.

The characteristics of the example are shown in Fig. 13. The case is that of a cylindrical tube under an internal pressure of $p = 0.6MPa$ and whose ends are fixed to diaphragms which allow displacements only in the longitudinal direction as illustrated in Fig. 13a. Besides, the following geometric and mechanical properties are adopted: length, $H = 600mm$; radius of tube, $R = 300mm$; thickness, $t = 3mm$; Poisson's coefficient, $\nu = 0.3$ and Young's modulus of elasticity, $E = 2.1 \times 10^5 MPa$.

The approximation space is generated from a uniform mesh of 4 Q3 elements and p-adaptive enrichment. Clouds of base nodes 3, 4 and 5 shown in figure 13(b) are enriched producing $p = 6$ while the remaining clouds are enriched producing $p = 3$. The enrichments are accomplished on linear and cubic partition of unity, Case A and Case B respectively by taking advantage of the one-dimensional description of the solution.

In order to underline the advantage presented by case B relative to case A, results of the observed shear stress resultants are shown since such resultants involve third order gradients of displacement solution. The numeric results are compared to those obtained analytically for thin shells.

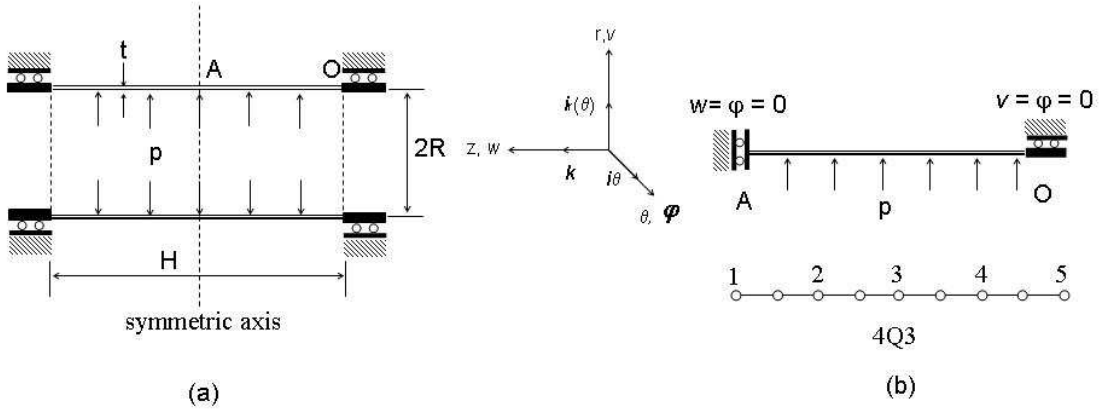

Figure 13: Cylindrical tube under uniform internal pressure.

As it can be observed in figure 14, the approximation spaces corresponding to enrichment of partition of cubic unity (Case B) supply the best results. In fact, such a partition makes it possible to obtain a highly regular solution due to the order of the solution polynomial ($C^1(\Omega)$-type space).

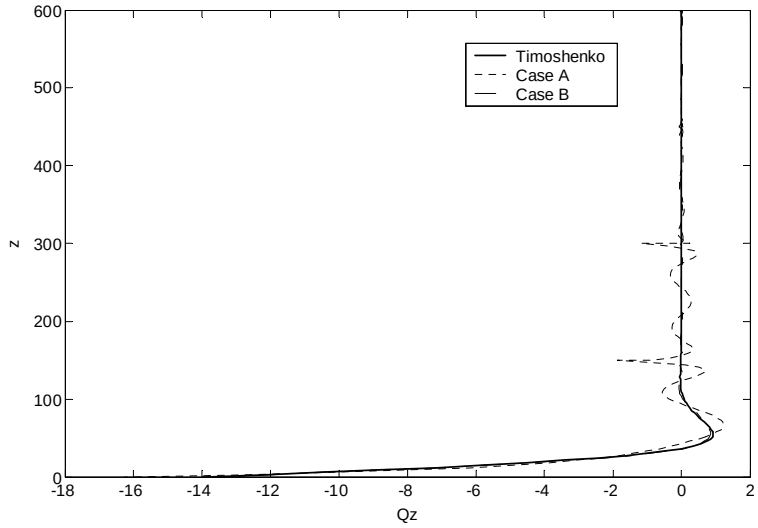

Figure 14: Behavior of shear stress resultant, Q_z along a meridian.

Spherical shell with top opening

Fig. 15 is an illustration of a shell (Grafton, Strome (1963), [8]) subjected to uniformly distributed unit bending moment ($m = 1\,in\,lb/in$) applied along its free top boundary.

For this example, the geometric and elastic properties are: mean radius, $R = 100\,in$; thickness, $t = 1\,in$; Young's modulus, $E = 10^7 psi$; Poisson coefficient, $\nu = 0.33$. The behavior of the shell is shown to be dominated by localized bending in the vicinity of the top border.

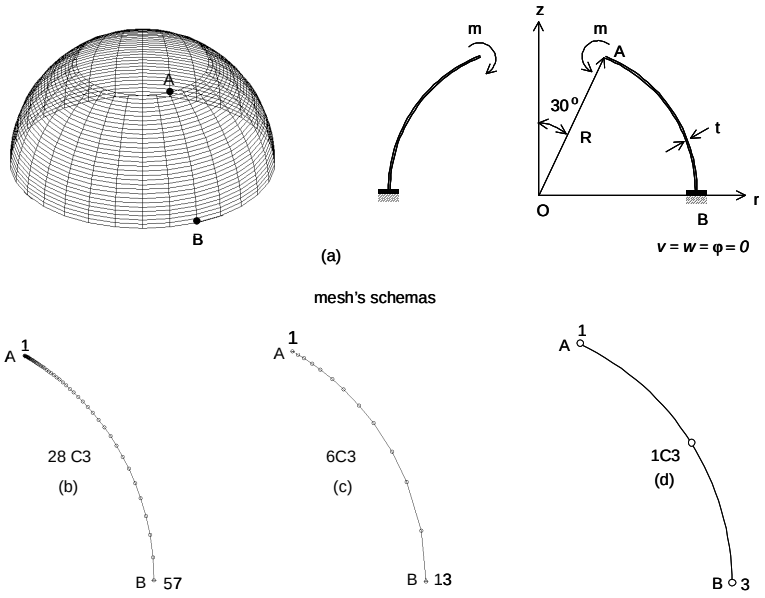

Figure 15: Hemispherical Shell with open top; a) adaptive mesh with 28 C3 elements; b) adaptive mesh with 6 C3 elements; c) mesh with 1 C3 element.

Both p and hp-adaptive refinements strategies were considered in the numerical analyses. The obtained results refer to displacement fields in the radial direction and distribution of the bending moment along a meridian (see Fig. 16). The elements used in this example, here designated by letter C3, make use of mappings according to relationships (9), (10) and (11).

Results of the proposed refinement strategies are compared with a reference solution obtained by adaptive hp-refinement with the following characteristic: a mesh of 28 C3-elements distributed following a geometric progression of factor 1.2 in the loading direction; clouds corresponding to nodes $\{1, 3, 5, 7, 9, 11\}$ enriched thus generating polynomial degrees of $\{1, 3, 5, 7, 9, 11\}$ and remaining clouds generating $p = 6$. In this case, the cubic partition of unity was enriched in order to guarantee better regularity of the reference solution.

The numerical resolution strategies tested have the following characteristics:

1. Case A: 1 C3-element mesh with enrichment of the cubic partition of unity which generates approximation polynomials $p = \{15, 14\}$ linked to the nodes $\{1, 3\}$.

2. Case B: A 6 C3-elements mesh using an *hp*-adaptive strategy in geometric progression of factor 1.5 and $p-$refinement on a linear partition of unity, generating $p = \{10, 10, 9, 8\}$ degrees approximations for clouds associated to nodes $\{1, 3, 5, 7\}$ and $p = 6$ for the remaining clouds.

The results shown in Fig. 16(a) and (b) demonstrate good performance of the proposed strategies. For the radius-thickness ratio used, the observed disturbances of bending moments at the borders can be captured without any need of $h-$refinement of the mesh as in the case of the strategy A. In this case, a high order adaptive $p-$refinement (105 degrees of freedom) on a cubic partition of unity ensures a satisfactory behavior and a continuous distribution of the bending moment along the meridian. The results obtained for strategy B demand 186 degrees of freedom. Because a linear partition of unity is used, the bending moment distribution, although very close of the reference solution, is found not to be continuous along the domain of the problem.

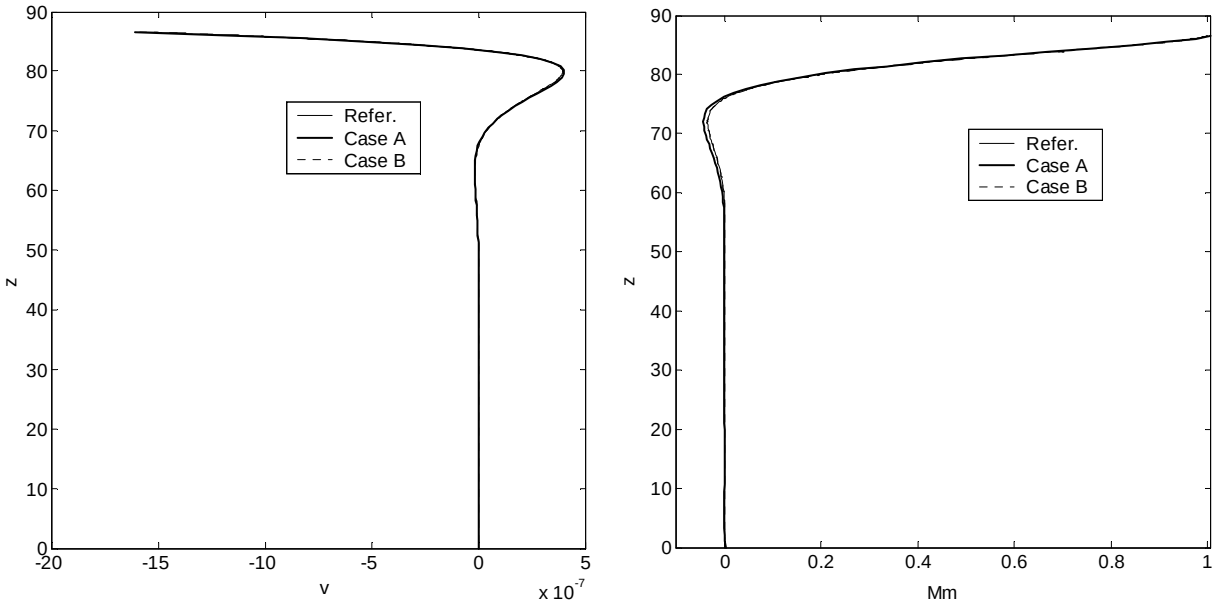

(a) (b)

Figure 16: a) Variation of transverse displacement, v along a meridian; b) Variation of the bending moment, M_m along a meridian.

6 Conclusions

Besides simplifying discretization, the approach, which considers the axis-symmetric character of several plate and shell problems, made it possible to explore, with an excellent performance, the p and hp-adaptive strategies. Such a resource is almost not possible in approximation spaces constructed in R^2 and R^3.

In the examples presented, those advantages are pointed out, particularly in the solution of problems involving numeric locking and strongly localized solutions problems without singularity.

On one hand, although the variational formulation adopted to describe the kinematics of shells resulting from the Reissner-Mindlin model is not 'a priori' free from locking, both the plate example and the example of a cylinder under punction showed that this type of problem can be satisfactory solved by approximation enrichment.

On the other hand, in localized solution problems, the selective enrichment tool made possible by the GFEM applied to one-dimensional spaces obviously without mesh distortion explore advantages such as the use of high order polynomials to enrich the approximations and construct them in real domain of the problem. Besides this, it was possible to construct, at a low computational cost, enriched solutions on partitions of unity with regularity $C^1(\Omega)$. Such an alternative allowed us obtain a continuous stress resultant distribution in the problem domain, a numeric problem not very well solved in shells.

In general, the observed performance of the spaces constructed by the GFEM was good for the problems proposed.

References

[1] S. Ahmad, B. M. Irons, and O. C. Zienkiewicz. Analysis of thick and thin shell structures by curved finite element. *International Journal for Numerical Methods in Engineering*, 2:419–451, 1970.

[2] J. L. Batoz and G. Dhatt. *Modélisation des structures par éléments finis. 3, Editions.* Hermés, Paris, 1992.

[3] T. Belytschko, Y. Lu, and L. Gu. Element free galerkin method. *International Journal for Numerical Methods in Engineering*, pages 229–256, 1994.

[4] C. A. Duarte, I. Babuska, and J. T. Oden. Generalized finite element method three dimensional structural mechanics problems. *Computers & Structures*, 77:215–232, 2000.

[5] C. A. Duarte and J. T. Oden. Hp-clouds – an h-p meshless method. *Numerical Methods for Partial Differential Equations*, 12:673–705, 1996.

[6] O. A. Garcia. *Plates and shells static analysis by the Generalized Finite Element Method.* Doctoral dissertation, Federal University of Santa Catarina, Florianópolis, 2003.

[7] E. J. Kansa. Multiquadrics-a scattered data approximation scheme with application to computational fluid dynamics i: surface approximation and partial derivative estimates. *Computer Mathematic Applications*, 19(8-9):45–127, 1990.

[8] H. Kraus. *Thin elastic shells*. John-Willey, New York, 1967.

[9] P. Krysl and T. Belytschko. Analysis of thin shells by the element-free galerkin method. *International Journal Solids Structures*, 33(20-22):3057–3080, 1996.

[10] S. Li, W. Hao, and K. W. Liu. Numerical simulations of large deformation of thin shell using meshfree methods. *Computational Mechanics*, 25:102–116, 2000.

[11] W. K. Liu, S. Jun, and Y. F. Zhang. Reproducing kernel particle method. *International Journal for Numerical Methods in Fluids*, 20:1081–1116, 1995.

[12] J. M. Melenk and I. Babuska. The partition of unity finite element method: Basic theory and applications. *Computer Methods in Applied Mechanics and Engineering*, 139:289–314, 1996.

[13] S. S. Da Nóbrega and S. P. B. Proença. Analysis of double curvature thin structures by non-conventional finite element method. In *Iberian Latin-American Congress on Numerical Methods in Engineering*, Guarapari, 2005.

[14] J. T. Oden and J. N. Reddy. *An introduction to the mathematical theory of finite elements*. John Wiley and Sons, New York, 1976.

[15] B. Szabó and I. Babuska. *Finite Element Analysis*. John Wiley &Sons, New York, 1991.

[16] S. P. Timoshenko and S. Woinowsky-Krieger. *Theory of Plate and Shells*. McGraw-hill book company, New York, second editions edition, 1959.

[17] X. Zhao, T. Y. Ng, and K. M. Liew. Free vibration of two-simply-supported laminated cylindrical panel via mesh-free kp-ritz method. *International Journal of Mechanical Sciences*, 46:123–142, 2004.